A General and Robust Active Fire Detection Method Using Sentinel-2 and Landsat Shortwave Infrared Measurements

Lu Gui, Rong Li, Minghui Tao, Zhe Jiang, Lunche Wang, Jun Wang, *Senior Member, IEEE*, Jiaxin Huang, Yi Wang, Liangfu Chen, and Santo V. Salinas

***Abstract*—Accurate detection of active fires (AFs) is crucial for improving estimates of biomass burning emissions and environmental management. Satellite remote sensing at shortwave infrared (SWIR) bands with 10–30 m spatial resolution has great potential in identifying the numerous small AFs missed by fire-monitoring systems using coarse spatial resolution data, but is challenging due to heterogeneous backgrounds and multiple interferences. By combining the enhanced threshold method and abundant prior information, we developed a generalized and robust fire detection algorithm using the daytime Sentinel-2 SWIR observations over complex surfaces in China. To discriminate with high reflecting surface targets such as rooftops and solar panels, more thresholds with visible and SWIR bands, along with land cover datasets, are used. Moreover, industrial thermal anomalies are excluded by time series satellite images. Validations of Sentinel-2 AF detection through visual inspection show very low commission rates (<1%–3%) over selected regions of the world. Since burned areas in fire boundaries with higher temperature than the background were taken as AFs, the average omission rates increase to ~3%–4%. A maximum omission rate of ~7%–8% occurs in African grassland, which has a short burning time. In spite of consistent spatial patterns, 1 km moderate resolution imaging spectroradiometer (MODIS) and 375 m visible infrared imaging radiometer Suite (VIIRS) detections performed in the medium infrared (MIR) bands missed more than 90% of Sentinel-2 AFs. With the flexible framework, our method also has robust performance in similar Landsat 8/9 SWIR observations. By combing Sentinel-2 2B/2C and Landsat 8/9 observations, our reliable AF detection at fine scales (20–30 m) can provide a significant supplement for the biomass burning emission estimation with a temporal resolution of 2–3 days.**

***Index Terms*—Biomass burning, detection algorithm, Sentinel-2 Multispectral Instrument (MSI), small fires.**

Received 22 June 2025; revised 1 September 2025, 10 November 2025, and 12 December 2025; accepted 16 December 2025. Date of publication 23 December 2025; date of current version 5 January 2026. This work was supported in part the National Natural Science Foundation of China under Grant 42171354 and Grant 42271382 and in part by CAS Project for Young Scientists in Basic Research under Grant YSBR-037. *(Corresponding authors: Rong Li; Zhe Jiang.)*

Lu Gui, Minghui Tao, Lunche Wang, Jiaxin Huang, and Yi Wang are with the Key Laboratory of Regional Ecology and Environmental Change, School of Geography and Information Engineering, China University of Geosciences, Wuhan 430074, China (e-mail: guilu@cug.edu.cn; taomh@cug.edu.cn; wang@cug.edu.cn; huangjx@cug.edu.cn; wangyi34@cug.edu.cn).

Rong Li is with the School of Resources and Environmental Science, Hubei University, Wuhan 430062, China (e-mail: rongli1015@126.com).

Zhe Jiang is with the Key Laboratory of Middle Atmosphere and Global Environment Observation, Institute of Atmospheric Physics, Chinese Academy of Sciences, Beijing 100029, China (e-mail: jiangzhe@mail.iap.ac.cn).

Jun Wang is with the Center for Global and Regional Environmental Research, The University of Iowa, Iowa City, IA 52242 USA (e-mail: jun-wang-1@uiowa.edu).

Liangfu Chen is with the State Key Laboratory of Remote Sensing Science, Aerospace Information Research Institute, Chinese Academy of Sciences, Beijing 100101, China (e-mail: chenlf@aircas.ac.cn).

Santo V. Salinas is with the Centre for Remote Imaging, Sensing and Processing (CRISP), National University of Singapore, Singapore 119076, Singapore (e-mail: crsscsv@nus.edu.sg).

This article has supplementary downloadable material available at https://doi.org/10.1109/TGRS.2025.3647717, provided by the authors.

Digital Object Identifier 10.1109/TGRS.2025.3647717

I. Introduction

OPEN biomass burning throughout global vegetation cover is a big threat to surrounding residents, with tremendous casualties and losses caused by large-scale wildfires every year. Moreover, these widespread burning, including both lightning and anthropogenic fires, emit a huge amount of greenhouse gases such as carbon dioxide (CO_2), carbon monoxide (CO), and methane (CH_4), and smoke particles contributing to a large fraction of global organic carbon (OC) and black carbon (BC) [1]. The elevated dense fire smoke with large transport potential can be blown thousands of miles away, which not only harms air quality and public health, but also has intense interactions with radiative energy balance, cloud, and biogeochemistry cycles. Owing to the abruptness and a certain randomness of these burnings in both spatial and temporal scales, global fire monitoring is fundamental in disaster management and emission estimation.

Satellite observations, thanks to global coverage, have enabled operational detection of biomass burning fires early since the 1980s [2]. By using the temperature difference between medium infrared (MIR) and thermal infrared (TIR) bands of the advanced very high-resolution radiometer (AVHRR), the bi-spectral algorithm was used to identify the location and timing of active fires (AFs) [3]. Since fixed thresholds can increase false alarms or omit smaller or cooler fires, the moderate resolution imaging spectroradiometer (MODIS) contextual algorithm makes use of dynamic thresholds by comparing signals of potential AF pixels with those of the neighboring ones in different windows [4]. Furthermore, fire radiative power (FRP) is largely used to characterize the fire combustion and emission rates [5]. However, the burnt area usually accounts for a very small fraction of the pixel size. Even fire detections performed using the MIR band, at 375 m spatial resolution, from the visible infrared imaging radiometer suite (VIIRS) detection tend to omit most of the small agricultural fires in regions such as eastern China (EC) [6], [7].

Thanks to higher spatial resolutions (20–30 m for Landsat 8/9 and Sentinel-2), satellite shortwave infrared (SWIR) observations have a great potential in identifying small AFs below the 375 m VIIRS detection limits (e.g., 100 m^2 for 375 m VIIRS at 1000 K) [8]. However, reflected solar radiation over high-reflecting surface targets, such as steel rooftops and solar panels, exerts multiple challenging interferences on fire detection at SWIR bands in daytime, especially in agricultural regions with dense populations. Furthermore, the numerous industrial thermal anomalies at fine scales are difficult to be separate from biomass burning fires directly with the radiation energy difference [9]. In addition, Sentinel-2 and Landsat 8/9 observations have a low revisit time (> 5–10 days) due to their narrow swath width, which should be combined.

The unique fine-scale measurements from satellites such as Landsat 8/9 and Sentinel-2 have motivated increasing efforts to develop SWIR fire detection algorithms [9], [10], [11], [12], [13]. Before the launch of Landsat 8 and Sentinel-2 satellite, a simple fixed threshold method with contextual test using SWIR bands of Advanced Spaceborne Thermal Emission and Reflection Radiometer (ASTER) achieved an accuracy of 80%–90% for AF detection at 30 m in the regions with dense fire activities [14]. More complex detection schemes were then proposed to detect AF using Landsat 8 operational land imager (OLI) at 30 m in selected scenes of the world [9]. Moreover, a multitemporal analysis is adopted to exclude fixed heat sources such as industrial hotspots and gas flares by their detection frequency. In spite of a very low (<0.2%) commission error rate (CR) (fraction of nonfire pixels mistaken as AF in the whole AFs) in selected scenes around the world, CR of Landsat 8 AF detection exceeds 34% in China with heterogeneous surface types [9]. Sentinel-2 multispectral instrument (MSI) AF detection at 20 m with adaptive thresholds in different fire-prone biomes achieved a low omission error rate of 4% on average [12]. By contrast, the mean CR of corresponding Sentinel-2 MSI AF detection is much higher (14%), and even exceeds 40% in complex surfaces. Tailored normalized hotspot indices based on radiance of two SWIR bands from combined Landsat 8/9 and Sentinel-2 measurements show reliable performance in wildfire mapping over forest regions [13], which can obtain a much higher temporal resolution of 2–3 days for global coverage [15].

The deep-learning (DL) methods have been used in Landsat/Sentinel-2 AF detections due to their powerful ability in modeling the nonlinear/high-order function relationships between satellite measurements and target parameters [16], [17], [18], [19]. Unfortunately, it is unfeasible to collect massive ground truths of the dynamic and transient fires manually matched with satellite measurements at 20–30 m. By annotating AF labels with detection results of threshold algorithms, Landsat 8 AF detection based on a convolutional neural network (CNN) achieved an average precision of ~87% [16]. Visual interpretations are further used to label interference objects, including building roofs, solar panels, and industrial heat sources in China, and only the U-Net type of CNN model is found to capture Landsat 8 AF boundary pixels fully and accurately [18]. It is worth noting that the training and validation of DL-based AF detection are conducted with satellite images covering very limited regions. More importantly, the AF label annotations of DL-based Landsat 8/9 and Sentinel-2 rely on detection results of the traditional threshold methods, which introduce their uncertainties before training [19]. By now, few works have given how the AF changes over space and time on a fine scale besides the limited scenes associated with DL methods training. Additionally, superresolution reconstruction with DL methods has been used to downscale daily VIIRS AF to the 30 Landsat 8 detection [20], which can obtain a more precise location of the AFs but cannot detect small/cool fires that only Landsat 8 can identify.

In spite of considerable uncertainties of current threshold methods, their flexible structures with clear physical principles have large potential for further improvement. Besides multiple bands, multitemporal information, and multiple a priori information can be used to both identify fires and filter interferences hierarchically and effectively. The highly reflective targets, such as rooftops and solar panels, are generally difficult to distinguish in the SWIR bands from small fires [21]. However, compared with the dynamic and transient fires, the artificial objects have distinct features such as fixed locations, visible colors, and geometric shapes [21]. While these features may not be fully identified by fire-related spectral bands and thresholds, there have been numerous classification datasets that can provide abundant prior information for AF detection [22], [23], [24], [25].

In this study, we present and test a new algorithm using Sentinel-2 MSI and Landsat 8/9 OLI SWIR data to improve the identification of small fires, with a primary focus on six regions of China that are more frequently affected by small fires, and with an overview of the algorithm performance provided over selected regions of the world. Section II introduces the current MODIS and VIIRS operational AF products and ancillary data used. The specific SWIR AF algorithm flow is described in Section III. Performance of Sentinel-2 and Landsat AF is validated with confirmed samples. Then, an intercomparison with MODIS and VIIRS AF products is conducted in EC. At last, the application potential and uncertainties of SWIR AF detection in global scale is discussed.

II. Datasets

A. Description of the Study Area

As shown in Fig. 1, open biomass burning is primarily concentrated in northeast, eastern, southwest, and southern China (SC), with straw burning and forest fires being the most common fire types. Agricultural activities are primarily located in the densely populated plains of the northeast and EC, with biomass burning also occurring in the mountainous and hilly regions surrounding the plains. Previous studies indicate that most farmland in China supports two or more harvests each year [26]. Postharvest of rice straw, wheat, maize, and other crops, agricultural residues are often burned in the field as a quick method of clearing the land. This practice has persisted

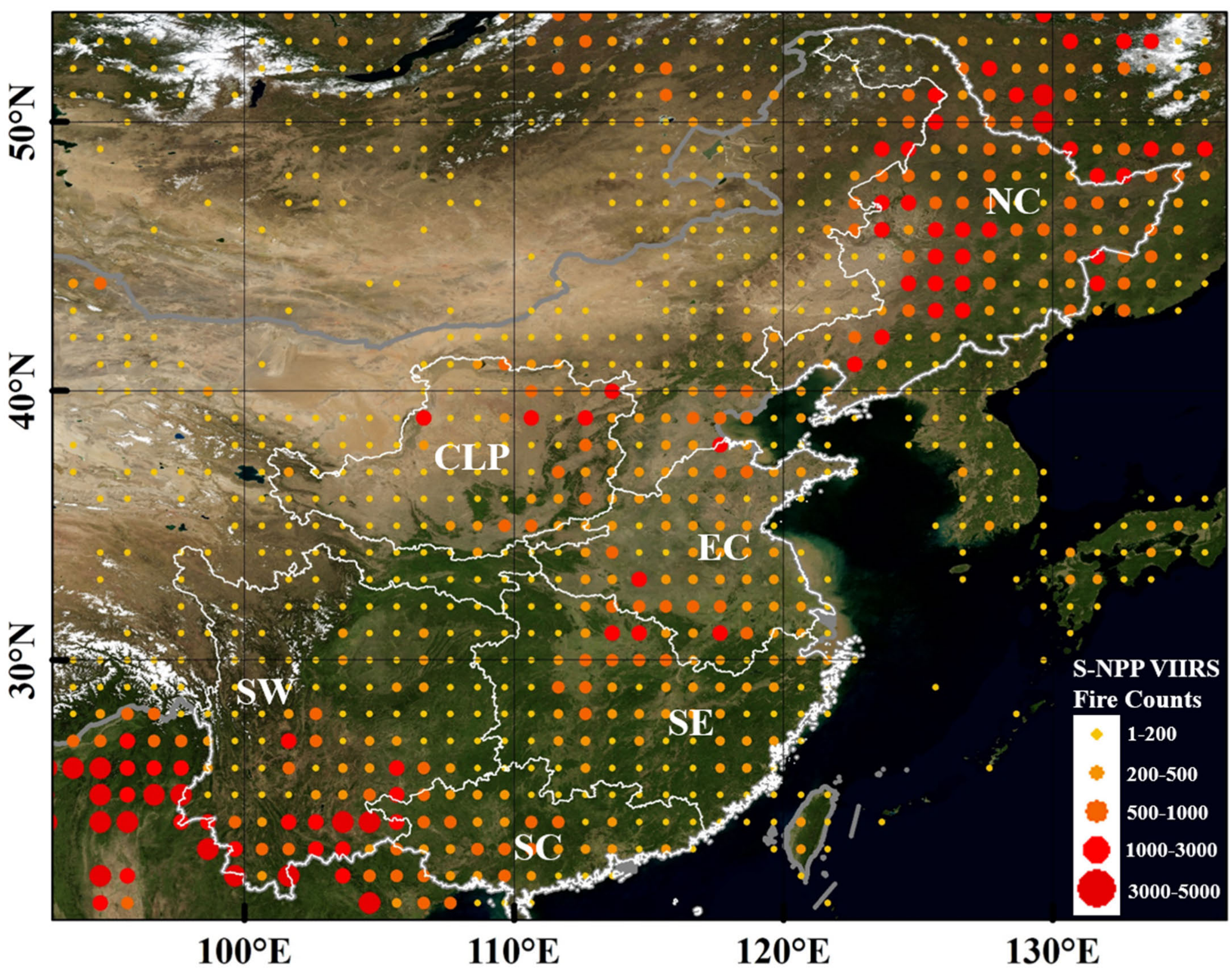

Fig. 1. Terrain of central and EC. The red dots represent the statistics of VIIRS fire pixels detected in each 1° grid cell during 2023. The solid white lines delineate the regions—NC, Chinese Loess Plateau (CLP), EC, Southern East (SE), Southern West (SW), and SC—selected for analyzing Sentinel-2 fire detection results based on the spatial distribution of VIIRS AFs.

in spite of being discouraged or prohibited since the late 1990s [26]. In SC, wildfires are common during the dry season, which spans from winter to early spring, when low humidity and drought conditions coincide with agricultural activities. Since extensive deserts and barren land are predominant in western China, we divided the main cropland in China into six distinct regions: northeast, Loess Plateau, EC, southeast, southwest, and SC. The overview of our algorithm performance is provided over selected regions of the world.

B. Sentinel-2 MSI and Landsat OLI Instrument

The European Space Agency (ESA) develops and operates the Sentinel-2 mission under the Copernicus program of the European Commission, aimed at collecting land observation data to support environmental services and disaster response [27]. The same MSI aboard Sentinel-2A (launched in 2015), Sentinel-2B (launched in 2017), and Sentinel-2C (launched in 2024) satellites capture optical images across 13 spectral bands covering visible (VIS), near-infrared (NIR), and SWIR spectrum, with spatial resolution of most bands at 10–20 m (Table I). As Sentinel-2A comes to the end of its operational life, combined Sentinel-2B and 2C observations with a swath width of 290 km can provide an extended revisit time of approximately five days near the equator and about 2–3 days at mid-high latitudes [15]. Sentinel-2 data are available on Google Earth Engine (GEE) as ortho-rectified images (UTM projection). The study used 22 493 tiles of Sentinel-2 MSI images from six regions, covering the second month of each season in 2022 and 2023 (January, April, July, October), obtained from GEE for the development of the AF detection algorithm.

The Landsat 8 and 9 satellites were launched in 2013 and 2021 respectively, with OLI and OLI-2 onboard measuring VIS, NIR, and SWIR radiation of the atmosphere-Earth system at a spatial resolution of 30 m. Besides the same spectral bands as OLI, OLI-2 has an enhanced 14-bit radiometric resolution. With a swath width of 185 km, Landsat 8/9 satellites together have an eight-day repeat cycle. Because of the similarity of spectral bands, we mainly analyzed Landsat 8/9 OLI data for the test of our method here.

C. Satellite AF Products

With a close time crossing the equator around 10:30 am local time as Sentinel-2, MODIS aboard Terra satellite

TABLE I
LIST OF SENTINEL-2 MSI CHANNELS USED IN THE AF DETECTION ALGORITHM

Sentinel-2 Bands	Central Wavelength (nm)	Spatial resolution (m)	Description
B1	443	60	Coastal aerosol
B2	490	10	Blue
B3	560	10	Green
B4	665	10	Red
B5	705	20	Vegetation Red Edge
B6	740	20	Vegetation Red Edge
B7	783	20	Vegetation Red Edge
B8	842	10	NIR
B8A	865	20	Vegetation Red Edge
B9	940	60	Water vapor
B10	1375	60	SWIR-Cirrus
B11	1610	20	SWIR
B12	2190	20	SWIR

since December 1999 provides operational AF products at 1 km [28]. The MODIS contextual algorithm analyses MIR and TIR brightness temperature coupled with reflectance at 0.86 μm to identify potential fire pixels [4], which can not only detect large or high-temperature fires using absolute thresholds, but also include smaller or cooler fires through statistical tests with background pixels [29]. The global commission errors (CR) for MODIS fire detections are very low with a CR of only 1.2% [29]. By contrast, there is a substantial increase in omission errors (OR) of MODIS AF in cropland with much smaller or cooler fires [30].

The first VIIRS instrument was launched aboard the Suomi National Polar-orbiting Partnership (S-NPP) satellite in October 2011 with an overpass time at 1:30 pm local time. With a higher spatial resolution of 375 m, VIIRS may detect smaller fires than MODIS [8]. To assess differences in the ORs, using sensors at different spatial resolutions, we compared Sentinel-2 AF with the Terra MODIS 1 km fire product (MCD14ML) and the VIIRS 375 m fire product (VNP14IMG) on Sentinel-2 imaging orbits during 2022 and 2023.

D. High-Resolution Satellite Images

High-resolution satellite images from GaoFen (GF)-1, GF-6, Google Earth, and uncrewed aerial vehicles (UAVs) were used to validate AF detection from Sentinel-2 SWIR measurements in typical cropland regions of China (Table S1). GF-1 and GF-6 satellites are equipped with panchromatic and multispectral sensors (PMSs), which provide panchromatic data at 2 m resolution and multispectral data at 8 m resolution. Google Earth images have high resolutions ranging from sub-meter to several meters. Moreover, UAV images offered resolutions as high as 0.1 m, providing clear evidence of biomass burning through the "black burn scar."

III. METHODS

To enhance the detection of small AFs, we developed a fire detection algorithm tested over some complex surfaces of China (Fig. 2). The detection begins with the identification of "candidate thermal anomaly pixels," which are potential indicators of fire activity. False alarms among these candidate pixels are then filtered with specific masks to establish a set of confirmed fire pixels. Specifically, the algorithm primarily uses the MSI Band 4 (Red), Band 8A (NIR), and Band 12 (SWIR) for fire detection, along with the other bands for masking clouds and water and excluding high-reflective objects.

A. Sentinel-2 MSI AF Detection

Step 1 (Identification of Potential AF Pixels): To identify potential AF pixels, a normalized index based on MSI band12 and band 8A is used. $\rho 12$ and $\rho 8A$ denote Sentinel-2 MSI reflectance at the top of atmosphere (TOA), respectively. The test (1) is designed to maximize the specific sensitivity to AFs and minimize the interference from artificial surfaces (Fig. S1) [31]. By statistical analysis from 369 MSI images in northern and SC, the index is robust to both flaming and smoldering fires with obviously higher temperature than the background

$$(\rho 12 - \rho 8A)/(\rho 12 + \rho 8A) > 0.5. \tag{1}$$

Based on GF5B hyperspectral satellite images (Fig. S2), surface reflectance in Red and NIR bands differs significantly in different surface types [21]. Test (2) is used to exclude interferences from impervious surfaces as much as possible. $\rho 4$ denotes Sentinel-2 TOA reflectance in band 4

$$-0.05 < (\rho 8A - \rho 4) < 0.15. \tag{2}$$

Step 2 (Mask of Clouds/Snow/Ice/Water): An effective cloud mask is essential for accurate AF detection [4]. To reduce AF omission under thin clouds, a threshold of less than 30% clouds was selected for the MSI images we used. Since the MSI cloud mask is conducted at 60 m resolution, some bright but small clouds can be neglected. To give a stringent mask of high-reflective clouds and snow/ice, a test is made as follows:

$$(\rho 3 - \rho 12)/(\rho 3 + \rho 12) < 0 \quad \rho 8A < \rho 11 \qquad \rho 12 > 0.5. \tag{3}$$

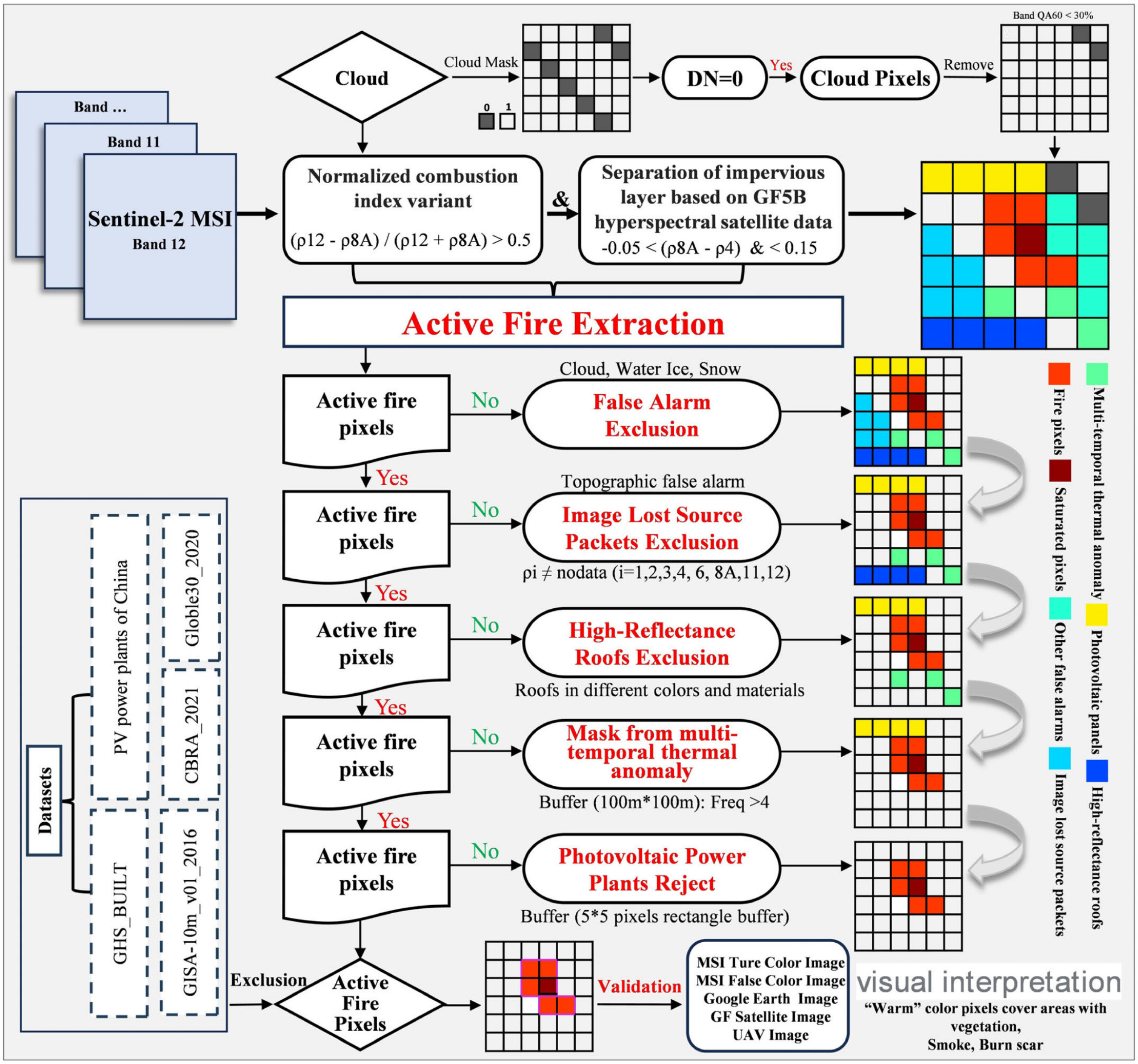

Fig. 2. Flowchart of the algorithm for detecting small fires over complex surfaces.

Water pixels were filtered out by testing using their strong absorption in the SWIR band as follows:

$$\rho 12 > 0.03. \tag{4}$$

Furthermore, seasonal bare lands on the slope can lead to false fire alarms, which can be excluded

$$\rho 1 > 0.1 \ \rho 2 > 0.1 \ \rho 3 > 0.1. \tag{5}$$

Step 3 (Mask of High-Reflectance Roofs): In densely populated EC, the high-reflectance roofs can significantly interfere with the accuracy of AF detection. Therefore, reflectance tests were conducted by selecting a large number of roofs in densely populated areas across Northeastern, Northern, and EC (Fig. S3). A series of masks (6)–(8) was made to reduce the false alarms caused by high-reflectance roofs of different colors and materials at SWIR bands.

Red Roofs

$$0 \le |\rho 3 - \rho 2| \le 0.05 \quad (\rho 4 - \rho 3)/\rho 3 > 0.5. \tag{6}$$

Blue Roofs

$$\rho 2 > \rho 3 \ \rho 2 > \rho 4 \ (\rho 2 - \rho 3)/\rho 3 > 0.2. \tag{7}$$

White Roofs

$$\begin{aligned} (\rho 2 + \rho 3 + \rho 4) > 0.6 \qquad & \rho 12 < 1| \\ (\rho 2 + \rho 3 + \rho 4) - \rho 12 > 0| & \\ (\rho 2 + \rho 3 + \rho 4) > 0.9 \qquad & \rho 12 < 1.4. \end{aligned} \tag{8}$$

Step 4 (Filtering Fixed Thermal Anomalies From Multitemporal Observations): The persistent thermal anomalies from industrial activities that burn fossil fuels were filtered out by their repeated detection frequency at the same location (Fig. S3). Specifically, MSI thermal anomaly pixels that appeared more than four times at the

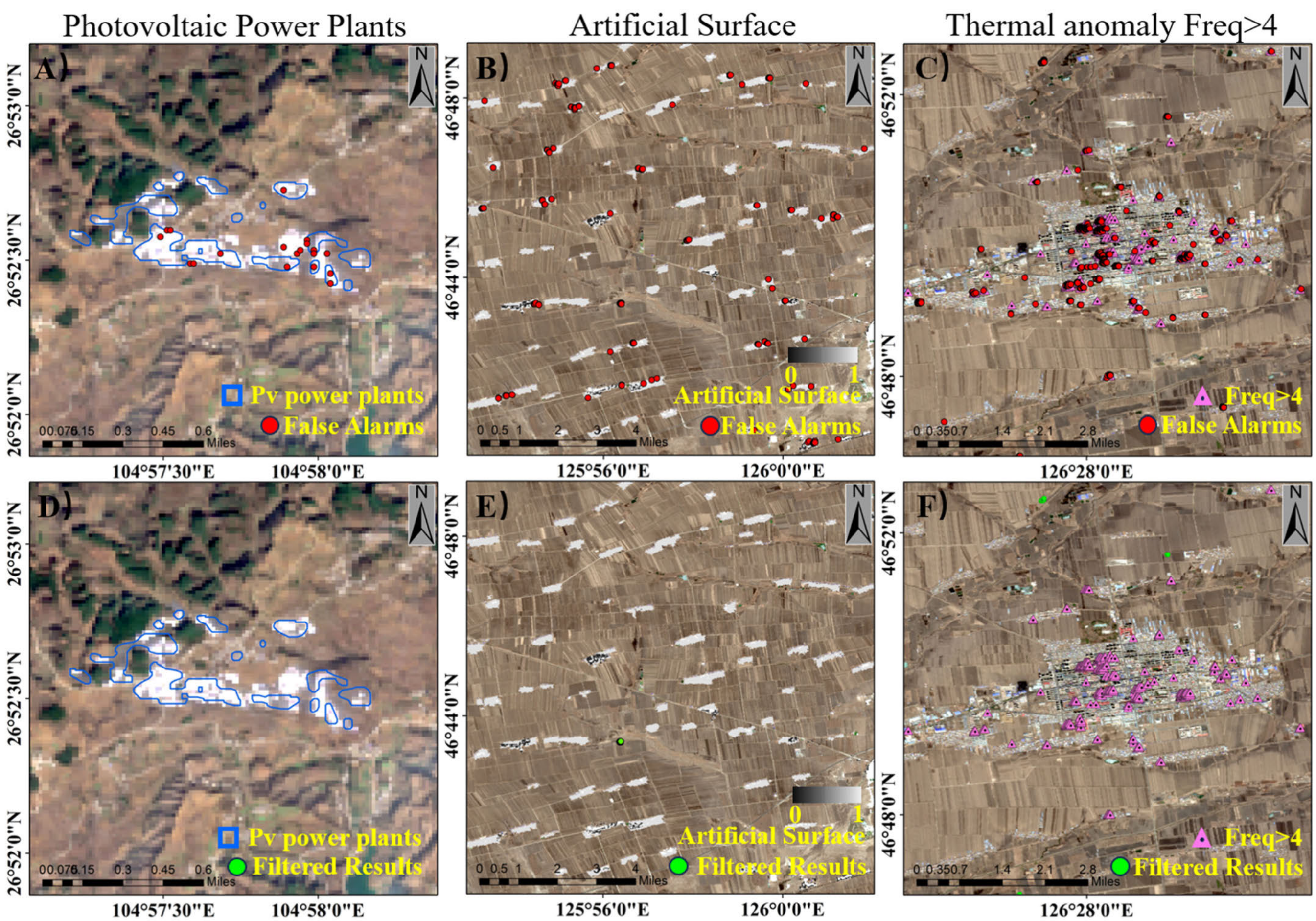

Fig. 3. Panels A–C show the spatial distribution of photovoltaic power plants, artificial surfaces, and high-frequency thermal anomalies, respectively. Panels D–F show the results after the filtering procedures.

same location were excluded [32]. A 100 m buffer was established around these pixels to further eliminate potential artificial interferences associated with these persistent anomalous pixels (Fig. S4a).

Step 5 (Mask of Other High-Reflectance Surface Objects): The specular reflection from solar panels of photovoltaic power stations and vegetable greenhouses can also severely interfere with SWIR AF detection [9], [10]. This phenomenon is especially common on hilltops and in open areas with full sunlight (Fig. S5). To filter out these high-reflectance objects, a 5 × 5 window with potential AF centered in was used. If any pixel within the window passed test, the central potential AF pixel was excluded as follows:

$$\begin{aligned}&\rho 4 > 0.5 \qquad \rho 3 > 0.5 \quad \rho 2 > 0.5 | (\rho 2 - \rho 4)/\rho 3\\ &\quad > 0.5 | \rho 8A > 0.5 \qquad \rho 12 > 1.2.\end{aligned} \tag{9}$$

Step 6 (Filtering False Alarms With Prior Land Classification Datasets): Compared with AFs that have great changes in location and size, land cover classification datasets have very robust performance in most scenes due to the fixed distribution of artificial objects. Besides threshold tests with MSI spectral reflectance, these prior land classification datasets provide a fundamental constraint of the nonvegetation surface types (Fig. 3). As shown in Fig. S4, external datasets such as "China Photovoltaic Power Plants" and impervious surface products can effectively exclude the interference from these permanent artificial objects.

B. Algorithm Assessment

Validation of open biomass burning at the global scale is challenging due to the scarcity of ground-based monitoring or high-resolution satellite data at Sentinel-2 overpass time. Here, we select cloud-free dates randomly to visually interpret AFs in typical surface type regions of the world with stricter discriminatory criteria in Fig. 2.

1) *Warm Colors:* False-color images (B12, B11, B8A) with "warm" colors (red or orange) are used to identify potential AFs with higher temperature than backgrounds, while nonfire backgrounds exhibit "cool" colors.
2) *Smoke:* A smoke plume over the vegetation area can visually verify a fire event.
3) *Burn Area:* A "black burn scar" in the MSI true color image can indicate a straw-clearing fire in the current or previous period.
4) *GF Images:* High-resolution satellite images or UAV RGB images can be used as supplements. Fig. S6 and S7 provide examples of the confirmed Sentinel-2 AFs in croplands and forests, respectively. AF detections that

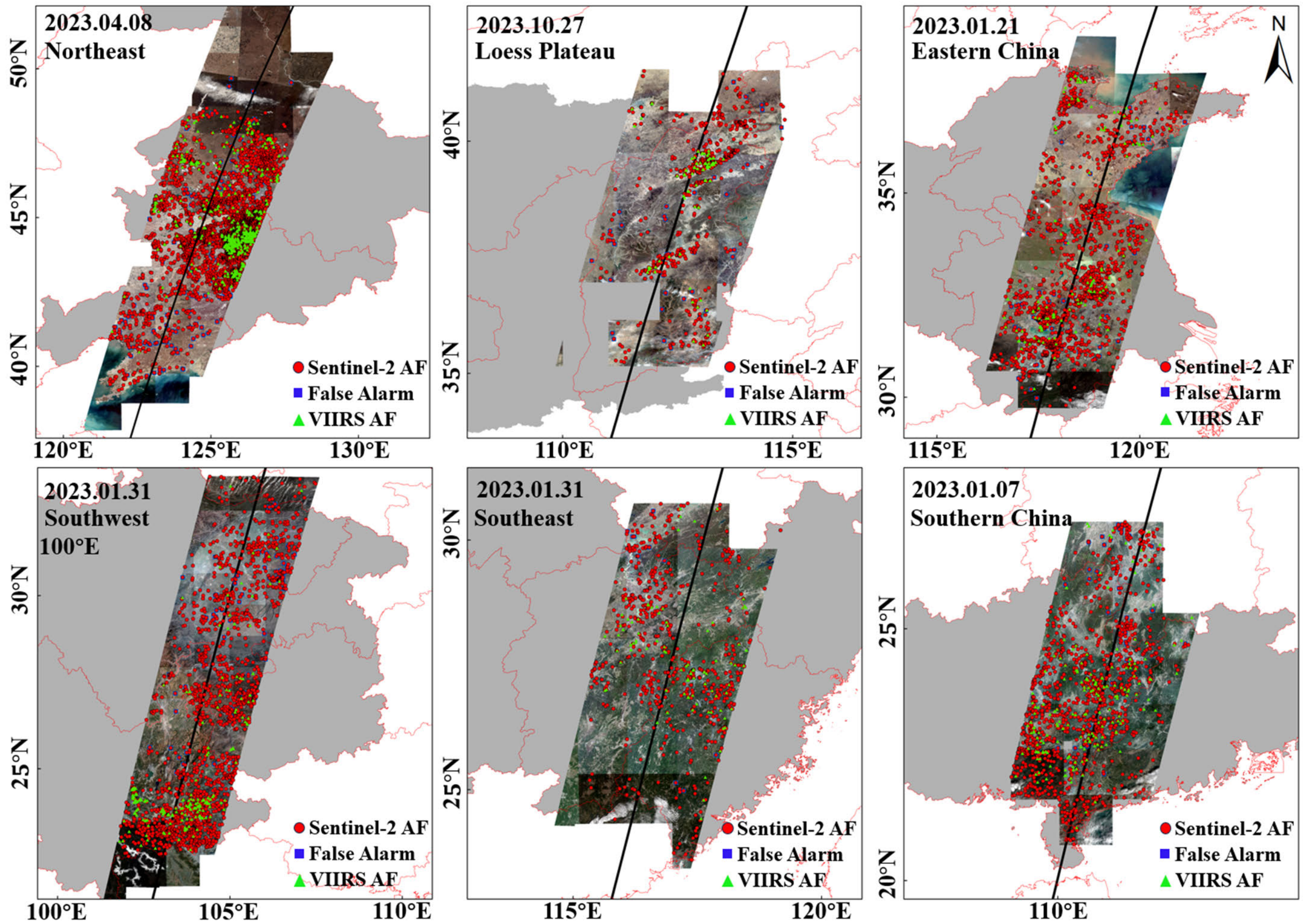

Fig. 4. Spatial distribution of MSI and VIIRS AFs in the six study areas.

do not correspond to true fire occurrences are defined as commission errors. By contrast, the true fires that were taken as nonfires in AF detection are considered as ORs.

C. Estimating Omission Rate of MODIS and VIIRS AF

MSI AF detection during 2022–2023 was compared with MODIS and VIIRS products on Sentinel-2 imaging orbits. ORs for MODIS and VIIRS AF data were estimated using the error matrix method, which assesses the overall classification accuracy of moderate-resolution satellite observations [33], [34]. Considering the distortion of VIIRS and MODIS pixel size at large viewing angles at the image edge [35], MSI AF detections within spatial windows of 1.5 and 0.5 km were used to match with and validate MODIS and VIIRS fire detection, respectively. Although numerous MSI AFs can exist within the spatial window, MODIS or VIIRS detection may omit most AFs with very a small size or cool temperature [36]. The OR of MODIS and VIIRS AF detection was calculated as follows:

$$\mathrm{OR} = \frac{Q}{N} \times 100\%. \tag{10}$$

Q is the number of MODIS or VIIRS scenes did not detect fires within the 1.5 or 0.5 km window that has MSI AFs fires, and N is the total number of 1.5 or 0.5 km windows that have MSI AFs.

IV. Results and Analysis

A. Sentinel-2 MSI AF Detection and Evaluation

Fig. 4 shows the comparison of MSI and VIIRS fire detection in typical scenes, including croplands, grasslands, and forests in northern and SC. In northern China with widespread croplands and dense villages, Sentinel-2 MSI AF detections have CRs ranging in ~1%–2% and ORs in ~1%–5%. Agricultural fires for straw cleaning are predominant in northern China, which usually have small areas (< 1000 m^2) and rapid burning process (within 1–2 h) with high temperature only lasting a short time (<half to 1 h). Compared with CR, the slightly higher ORs can be caused by the burned fires around the burning region boundaries. For validation of MSI detection, burned fire pixels with a higher temperature than the background are considered as AFs. Sentinel-2 MSI with higher spatial resolution detected nearly 50 000 AF pixels in northeast China (NC) on April 8, 2023, among which 483 were false alarms, with a CR of approximately 1%. In contrast, VIIRS detected only 857 AF pixels, with an OR of 94.55%. As shown in Fig. S6, most cropland fires can be missed due to their small size or cool temperature by the 375 m VIIRS fire products. Sentinel-2 detections provided a more detailed map of burning fires and combustion phase, including the spreading fire front, owing to their 20 m spatial resolution.

In SC, MSI AF detections have very low CRs in 0.2%–1% and ORs in 1%–4% (Fig. 4). The increase of MSI AF detection

TABLE II

DETAILED DESCRIPTIONS OF FIRE DETECTION RESULTS IN SIX STUDY AREAS. "OUTPUTS" REFERS TO ALL AF CANDIDATES GENERATED BY THE ALGORITHM PRIOR TO SCREENING. "FILTERED RESULTS" REPRESENT DETECTIONS RETAINED AFTER APPLYING THE FILTERING PROCEDURES. "FALSE ALARMS" DENOTE NONFIRE THERMAL ANOMALIES. "CR" IS THE COMMISSION RATE, DEFINED AS THE RATIO OF FALSE ALARMS TO THE TOTAL OUTPUTS. "FILTERED CR" AND "FILTERED OR" CORRESPOND TO THE COMMISSION AND OMISSION RATES AFTER FILTERING, RESPECTIVELY. "ACCURACY" INDICATES THE OVERALL CORRECTNESS. "VIIRS AF" DENOTES THE TOTAL NUMBER OF VIIRS FIRE DETECTIONS, WHILE "VIIRS OR" REPORTS THE OMISSION RATE OF VIIRS RELATIVE TO SENTINEL-2 FIRE DETECTIONS. "MAIN FIRE TYPE" INDICATES THE DOMINANT FIRE TYPE WITHIN EACH REGION

	North East	Loess Plateau	Eastern China	South West	South East	Southern China	ALL
Data	2023.04.08	2023.10.27	2023.01.21	2023.01.31	2023.01.31	2023.01.07	/
Outputs	68274	6053	10415	7042	7366	10323	109473
Filtered Results	47911	5034	7479	6531	6567	9517	83039
False Alarms	483	108	108	175	19	59	952
CR	30.53%	18.62%	29.23%	9.74%	11.11%	8.38%	25.02%
Filtered CR	1.01%	2.15%	1.44%	2.68%	0.29%	0.62%	1.15%
Filtered OR	5.45%	4.02%	1.94%	1.97%	1.02%	1.19%	3.97%
Accuracy	98.99%	97.85%	98.56%	97.32%	99.71%	99.38%	98.85%
VIIRS AF	857	128	172	484	142	284	2067
VIIRS OR	94.55%	93.48%	98.78%	98.25%	77.81	75.02%	91.60%
Main Fire Type	Crop Fire	Crop Fire	Crop Fire	Forest Fire	Forest Fire	Forest Fire	/

accuracy in SC is ascribable to the higher intensity of forest fires. Most false alarms are caused by the high-reflectance rooftops. Our filtering procedure has effectively reduced the CR from ~8% to 30% to only ~0.2%–1% (Table II). Notably, the number of small fire pixels detected by Sentinel-2 was much higher than those by VIIRS and MODIS, with OR ranging from 75.02% to 98.78% (Table II). Compared with MODIS and VIIRS, the MSI can provide a clear fine-scale distribution of the forest fire fronts (Fig. S7).

To compare our algorithm with other methods using Sentinel-2 or Landsat 8/9 data in detecting small-area/cool-temperature AF, we selected Shandong province with predominated croplands, densely populated cities, and villages as a test region (Fig. 5). During October 2023, the straw burning of corn after harvest is prevalent in Shandong. Pixel-by-pixel validation using Google Earth images, GF images, and UAV images demonstrated that the average CR of our detection for straw burning is as low as 3.57% with a total number of 1564 AF pixels (Fig. S8). In spite of much larger numbers, other methods have very high CRs with Sentinel-2 detection in Liu (83.47%), and Landsat 8 detections in Schroeder (84.02%) and Murphy (92.91%) due mainly to the poor consideration of interferences from high-reflectance surface objects at SWIR bands [9], [11], [21]. It should be stated that these works only provided the CR of their AF detections. By masking the diverse high-reflectance surface objects with multiple thresholds and prior information, our algorithm achieves a very high accuracy in detecting small agricultural fires (Table S2).

B. Intercomparison With MODIS and VIIRS AF Products

To compare the spatial patterns of satellite AFs in different detection resolutions, Fig. 6 illustrates the seasonal frequency of three AF results across the study area in China for 2022 and 2023. Because of a much higher spatial resolution, the spatial occurrence rate of MSI AF is substantially larger than that of VIIRS and MODIS. The biomass burning hotspots have shifted from northern China in the summer to northeast during the spring and autumn [6]. Although the seasonal occurrence of fires detected by MSI, MODIS, and VIIRS varies significantly in magnitude, the spatial distribution patterns remain consistent across regions.

Fig. 7 shows the intercomparison of MODIS, VIIRS, and MSI fire detection ability in different scales. For relatively large and intense forest fire events, there is strong spatial consistency between the AF detected by MSI, MODIS, and VIIRS. However, MODIS and VIIRS AF cannot provide the

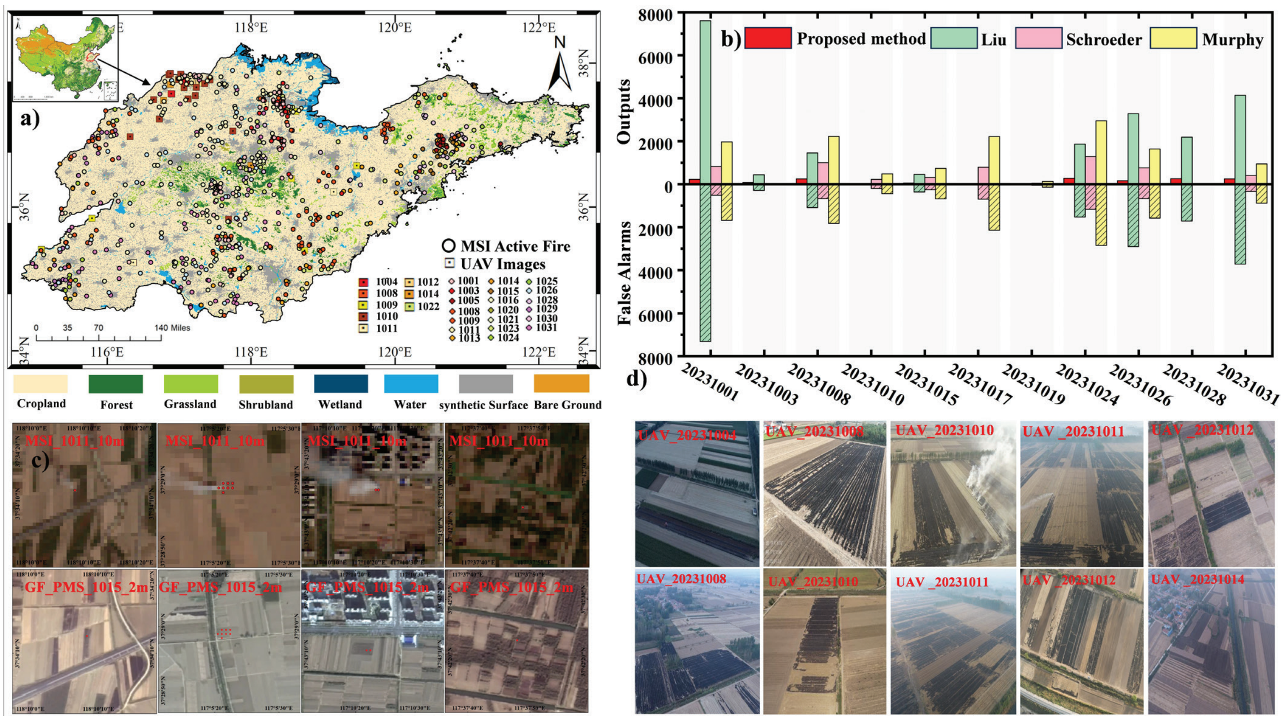

Fig. 5. (a) Spatial distribution of straw burning in Shandong Province during October 2023 based on Sentinel-2 MSI. (b) Number of candidate fire detections and false alarms produced by the proposed method (red), and the Liu (green), Schroeder (pink), and Murphy (yellow) methods in October 2023 when both Sentinel-2 and Landsat 8 observations were available. (c) Validation with 2 m GF satellite images. (d) Validation with UAV images.

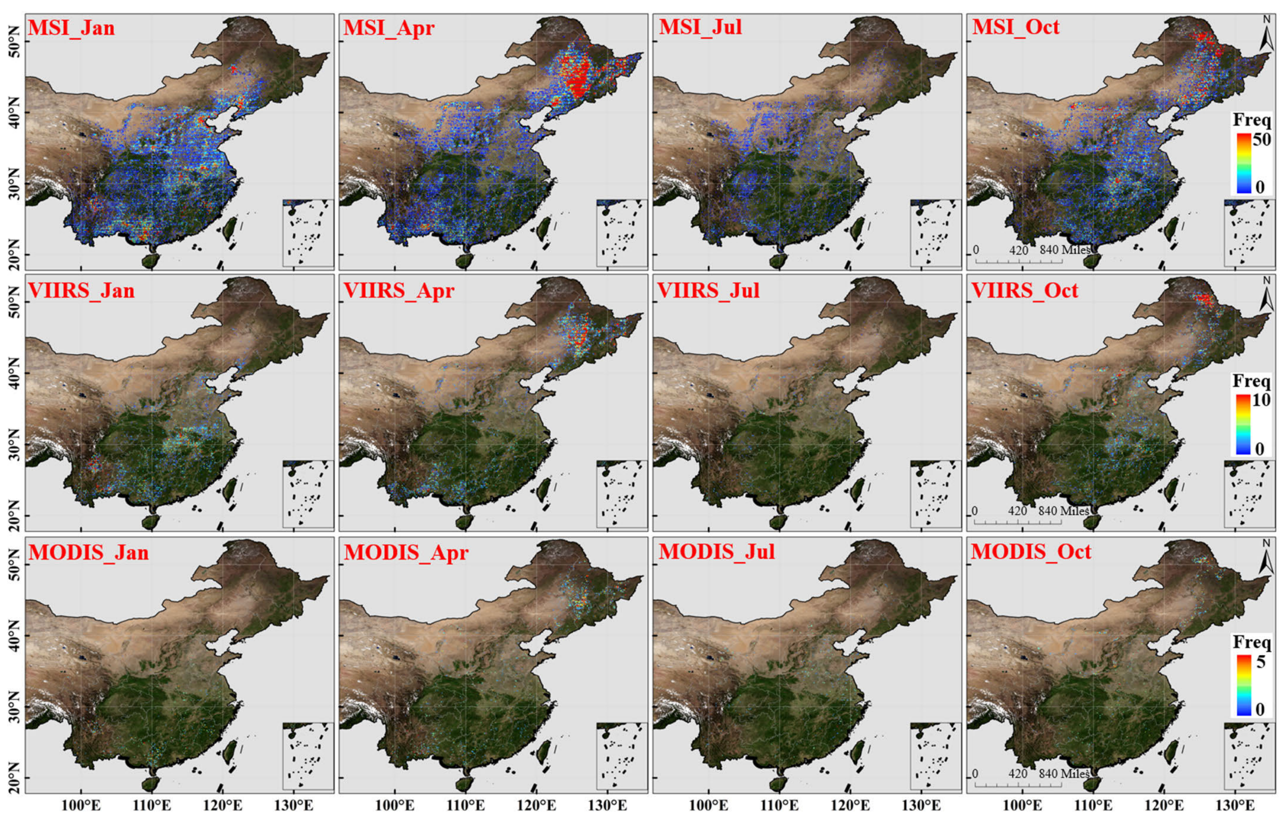

Fig. 6. Seasonal occurrence of 20 m MSI, 375 m VIIRS, and 1 km MODIS AFs on the Sentinel-2 imaging orbits in Central and EC during 2022 and 2023.

precise location of the actual fires and the detailed distribution of fire fronts as MSI. As the scale of forest fires gets smaller, MODIS detection begins to miss the AFs. Meanwhile, VIIRS detection exhibits a larger omission for the scattered cropland fires with smaller areas and cooler temperatures, which can only be detected by MSI.

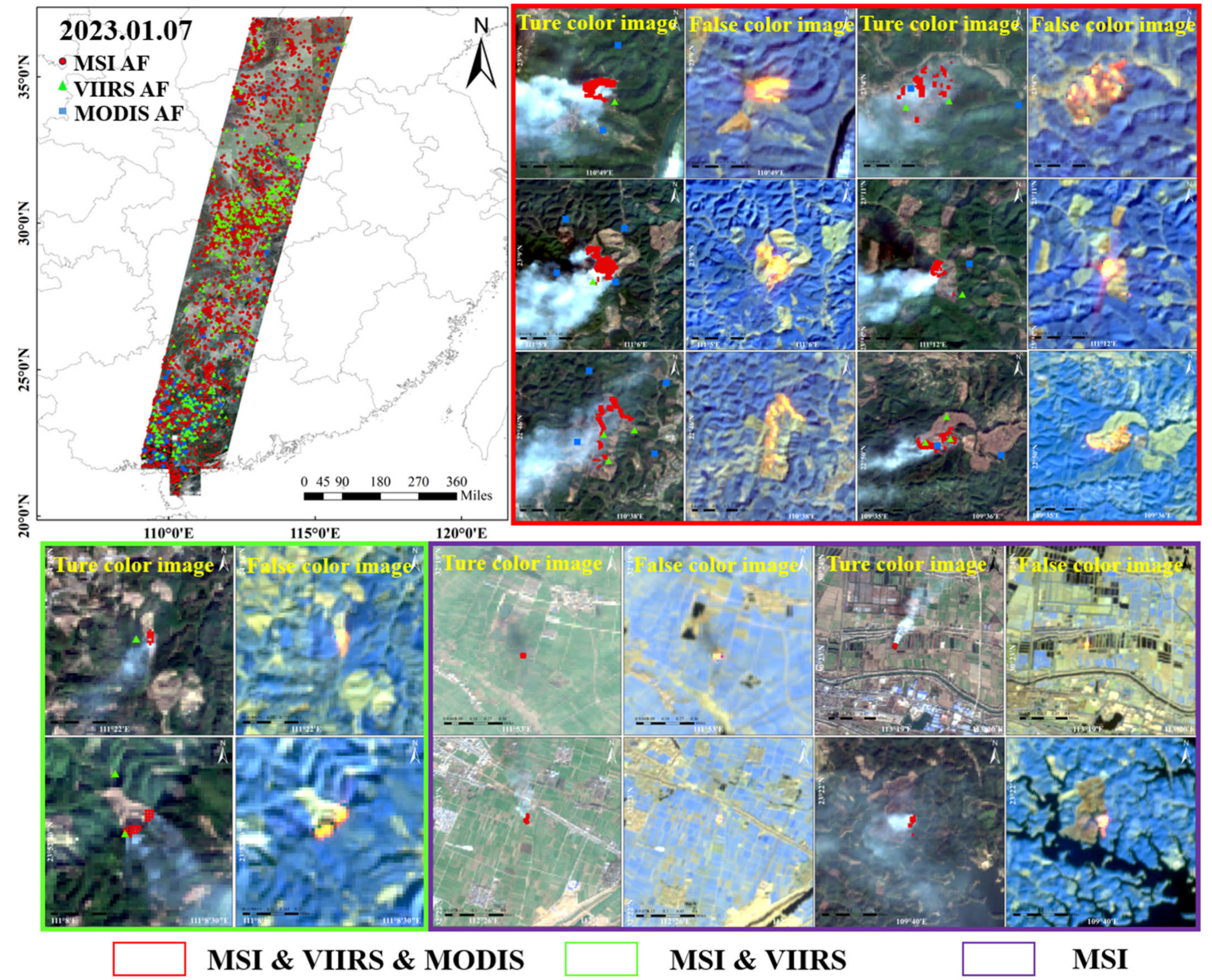

Fig. 7. Spatial distribution of AFs detected by MSI, VIIRS, and MODIS for fire events of different sizes.

As shown in Fig. 8, the MODIS detection missed 555 706 AFs identified by MSI detection with our method, with an overall OR of 94.47%. The VIIRS observations did not detect 556 120 AFs identified by MSI, with an overall OR of 94.86%. The ORs of VIIRS and MODIS AF detection are very close, which are caused by the fact that several missed AFs by VIIRS is only taken as one in the coarser MODIS pixel. There is little difference in the average OR in 2022 and 2023 (Fig. S9). The OR of both VIIRS and MODIS AF followed a seasonal trend, with the highest OR rates near 100% in the summer, which can be mainly caused by less combustion fuel and shorter burning time of wheat and rice straws. It should be stated that Sentinel-2 satellites pass over the equator about 2–3 h earlier than VIIRS. Most Sentinel-2 AFs can be burned out when VIIRS passes, and a considerable fraction of VIIRS AFs can be new fires in the corresponding time (Fig. S10). On the other hand, comparison of VIIRS and MSI detection shows that the total number of VIIRS AFs is less than 10% of those confirmed by MSI in matched grids (Fig. 4).

C. Applicability in Landsat 8/9 Detection and Global Scale

With the flexible framework, our method can be directly expanded to similar satellite instruments and other regions of the world. With similar wavelengths as Sentinel-2 MSI, Landsat 8/9 OLI AF detection with our method also achieved very low CRs (~1%–4%) and ORs (~5%–8%) over northeastern, central, and SC with different surface backgrounds and cropland types (Figs. S11–S13). Compared with Sentinel-2 MSI, the slight decrease in Landsat 8/9 OLI AF detection accuracy can be partly caused by the coarser pixel resolution. The combination of Sentinel-2B/2 C and Landsat 8/9 observations can increase the temporal resolution of global fine-scale (20–30 m) AF detection to ~2–3 days [15], which can improve the common underestimation of biomass burning emissions.

Thanks to robust performance in heterogeneous surface types and small-area/cool-temperature fires, Sentinel-2 AF detection with our algorithm can be directly used in other typical regions of the world (Fig. S14). Unlike most studies with validations only in certain image scenes, Sentinel-2 AF detections with our method have very low CRs (0.1%–3%)

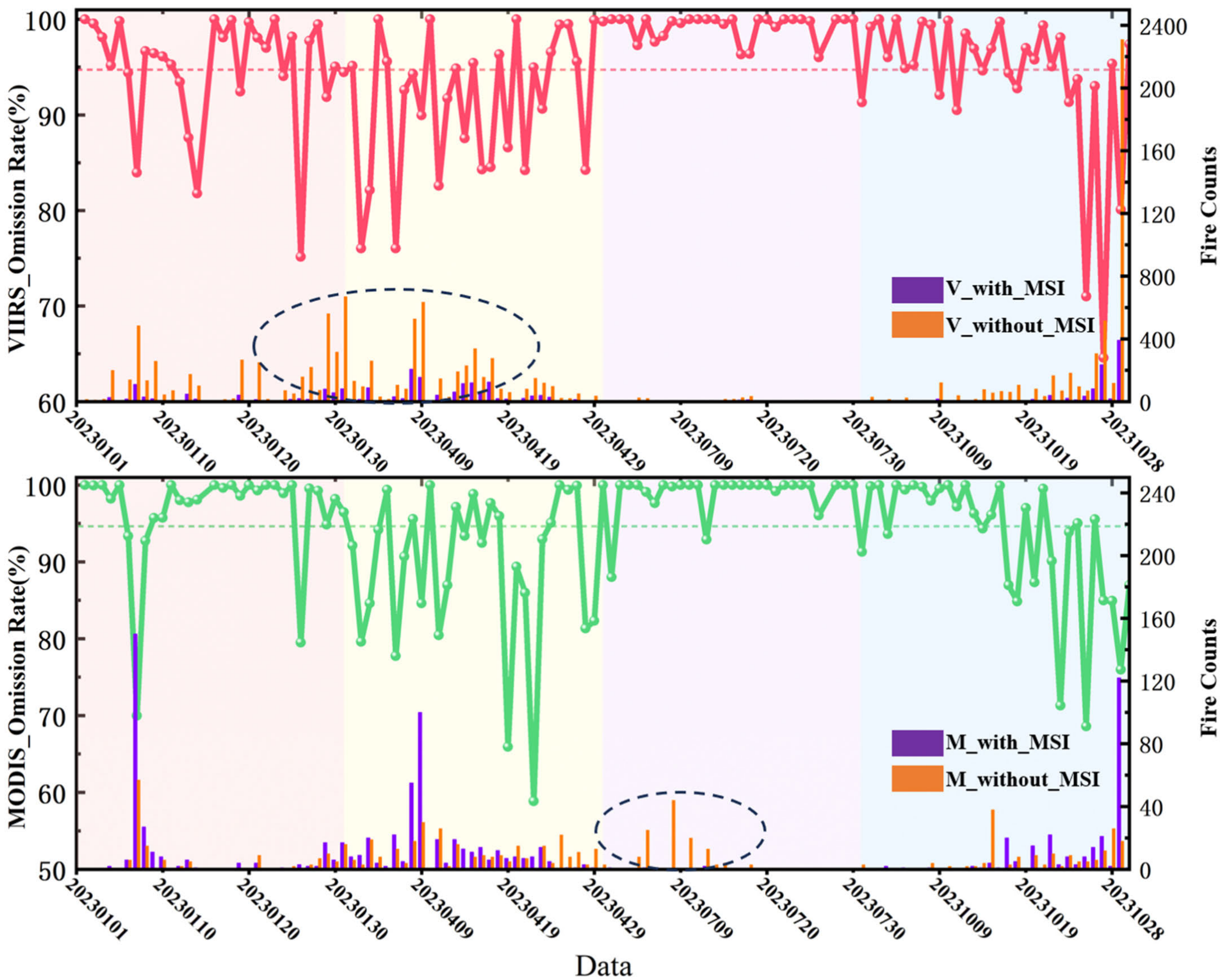

Fig. 8. Daily omission rates of AF detections from VIIRS and MODIS on Sentinel-2 imaging orbits in 2023. In this context, "V_with_MSI" denotes AFs detected by both VIIRS and MSI, while "V_without_MSI" refers to fires detected by VIIRS but not by MSI. The red/green horizontal dotted line represents the annual average of the MSI AFs omitted by VIIRS or MODIS.

and ORs (2%–8%) in all the randomly selected regions of the world (Fig. 9). In spite of enhanced thresholds and prior information used, a few of commission errors can occur in the croplands due to inference such as seasonal bare lands or temporary artificial objects. Most omissions occurred in fire boundaries, indicating that the actual ORs can be lower due to ambiguous identifications in the validation with looser thresholds. For AF detection, little looser thresholds can lead to an obvious increase of CRs. The maximum ORs (8.64%) of MSI detection occurred in the African grassland, where rapidly burned areas with slightly higher temperature than the background can be taken as AFs in our validation. Similar to the performance in China, MSI AF detection has a very high accuracy in the forest regions and a slight decrease in croplands with complex backgrounds.

V. Discussion

By combining the enhanced threshold method with the abundant prior information, Sentinel-2 MSI AF detection has been significantly improved. Unlike previous studies that only train and validate detection algorithms with a few satellite images covering very limited scenes, here we expand Sentinel-2 AF detection to the whole mainland of China and examine their spatial patterns at a fine scale of 20 m for the first time. The traditional fixed thresholds AF detection can hardly distinguish the prevalent interferences from heterogeneous surface backgrounds with diverse fire types and is subject to surface types, spatial resolution of satellite instruments, and clouds (Fig. S15). The introduction of prior information, such as the land cover datasets from Sentinel-2 MSI measurements, can provide a clear classification of the nonvegetation regions, which enables a robust performance of our threshold method. As shown in both previous threshold and DL-based methods, their AF detections can easily have a perfect performance over vegetation regions, such as forest without the interferences of artificial objects, but usually perform poorly in regions with heterogeneous surface types, such as in EC. In spite of a low temporal resolution of ~5 days, Sentinel-2 MSI can detect

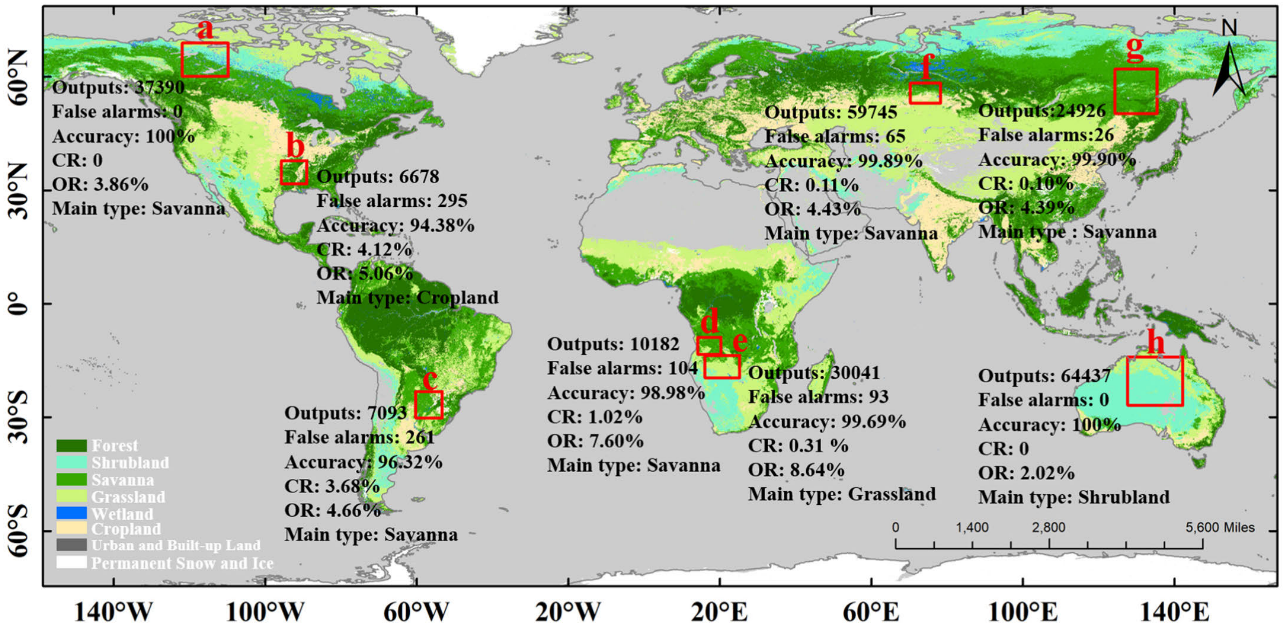

Fig. 9. Global geographic distribution of selected regions for validating AF detections from the Sentinel-2 MSI algorithm.

many more small-area or cool-temperature AFs than VIIRS and MODIS, which have been missed by current operational satellite AF products.

The robust and high accuracy at a global scale demonstrates a clear applicability of our method to provide operational fine-scale AF detection by making use of combined Sentinel-2B/2 C and Landsat 8/9 observations, as well as similar satellites. The global coverage of these combined satellite detections within ~2–3 days can greatly reduce the substantial omission of prevalent small-area/cool-temperature fires in VIIRS and MODIS products. To provide regular global products associated with large amounts of satellite datasets, our method can be run on the GEE platform, and more accurate a priori information can be used to better exclude interferences in complicated conditions. For emission estimation, a fire radiation power parameter at the SWIR bands should be developed in the future.

VI. Conclusion

The biomass burning emissions have been largely underestimated due to the omission of most small fires by coarse resolution of satellite detection. To enhance Sentinel-2B/2C and Landsat 8/9 AF detection at fine scale over complex surfaces, we developed a robust and high-accuracy algorithm by combining improved thresholds and prior constraints. To mitigate the common interference problem caused by high-reflectance targets, VIS and SWIR measurements and land cover dataset are used. Meanwhile, time series MSI images are used to further exclude the persistent industrial thermal anomalies. Validations of AF detection using randomly selected images in typical regions of the world, including croplands, grassland, and forests have very low CR (0.1%–3%) and ORs (2%–8%). The actual ORs of Sentinel-2B/2C and Landsat 8/9 detection can be lower due to ambiguous discriminations in fire boundaries taken as AFs in the validation. Burned fires with only slightly higher temperature than background pixels cannot be totally detected by our methods, since little looser thresholds can lead to a large increase of CRs.

With combined Sentinel-2B/2C MSI and Landsat 8/9 OLI observations, our method can provide an operational AF detection globally within 2–3 days, which can greatly improve fire management and the underestimation of biomass burning emissions. By contrast, more than 90% of Sentinel-2 AFs are missed by MODIS and VIIRS products, which are either too small or too cool for their coarse resolution. To support fire emission estimation, an FRP retrieved from SWIR observations will be developed in the future. The SWIR detections are mainly performed in daytime due to the scarcely available nighttime Landsat 8/9 data, which can have great potential in AF detection if more nighttime observations are conducted in the future satellite missions. To further enhance the data coverage, the Sentinel-2B/2C MSI and Landsat 8/9 OLI detection of burned area can be used as a supplement of the fires out of their passing time.

Data Availability

The new code link is: https://code.earthengine.google.com/15eace03767b83992d26231e240175a0. And the data will be made available on request.

Acknowledgment

The authors thank European Space Agency (ESA), United States Geological Survey (USGS), and Google Earth Engine (GEE) for providing all Sentinel-2 Multi Spectral Instrument (MSI) data. They would like to thank NASA's Fire Information for Resource Management System (FIRMS) for providing the Moderate Resolution Imaging Spectroradiometer (MODIS)/Visible Infrared Imaging Radiometer Suite (VIIRS) active fire (AF) data (https://firms.modaps.eosdis.nasa.gov/). And Satellite Application Center for Ecology and Environment, Ministry of Ecology and Environment (MEE) for providing GaoFen (GF) images. Zhe Jiang was supported via a grant from State Key Laboratory of Resources and

Environmental Information System. Jun Wang' s participation is made possible via in-kind support (Lichtenberger Chair professorship) from U. Iowa.

References

[1] C. Wiedinmyer et al., "The fire INventory from NCAR (FINN): A high resolution global model to estimate the emissions from open burning," *Geosci. Model Develop.*, vol. 4, no. 3, pp. 625–641, Jul. 2011.

[2] M. J. Wooster et al., "Satellite remote sensing of active fires: History and current status, applications and future requirements," *Remote Sens. Environ.*, vol. 267, Dec. 2021, Art. no. 112694.

[3] J. Dozier, "A method for satellite identification of surface temperature fields of subpixel resolution," *Remote Sens. Environ.*, vol. 11, pp. 221–229, Jan. 1981.

[4] L. Giglio, J. Descloitres, C. O. Justice, and Y. J. Kaufman, "An enhanced contextual fire detection algorithm for MODIS," *Remote Sens. Environ.*, vol. 87, nos. 2–3, pp. 273–282, Oct. 2003.

[5] M. J. Wooster, G. Roberts, G. L. W. Perry, and Y. J. Kaufman, "Retrieval of biomass combustion rates and totals from fire radiative power observations: FRP derivation and calibration relationships between biomass consumption and fire radiative energy release," *J. Geophys. Res., Atmos.*, vol. 110, no. D24, Dec. 2005, Art. no. D24311.

[6] J. Chen et al., "Overview of the performance of satellite fire products in China: Uncertainties and challenges," *Atmos. Environ.*, vol. 268, Jan. 2022, Art. no. 118838.

[7] C. Filizzola et al., "RST-FIRES, an exportable algorithm for early-fire detection and monitoring: Description, implementation, and field validation in the case of the MSG-SEVIRI sensor," *Remote Sens. Environ.*, vol. 186, pp. 196–216, Dec. 2016, doi: 10.1016/j.rse.2016.08.008.

[8] W. Schroeder, P. Oliva, L. Giglio, and I. A. Csiszar, "The new VIIRS 375 m active fire detection data product: Algorithm description and initial assessment," *Remote Sens. Environ.*, vol. 143, pp. 85–96, Mar. 2014, doi: 10.1016/j.rse.2013.12.008.

[9] W. Schroeder, P. Oliva, L. Giglio, B. Quayle, E. Lorenz, and F. Morelli, "Active fire detection using Landsat-8/OLI data," *Remote Sens. Environ.*, vol. 185, pp. 210–220, Nov. 2016, doi: 10.1016/j.rse.2015.08.032.

[10] S. S. Kumar and D. P. Roy, "Global operational land imager Landsat-8 reflectance-based active fire detection algorithm," *Int. J. Digit. Earth*, vol. 11, no. 2, pp. 154–178, Feb. 2018.

[11] S. W. Murphy, C. R. de Souza Filho, R. Wright, G. Sabatino, and R. Correa Pabon, "HOTMAP: Global hot target detection at moderate spatial resolution," *Remote Sens. Environ.*, vol. 177, pp. 78–88, May 2016, doi: 10.1016/j.rse.2016.02.027.

[12] X. Hu, Y. Ban, and A. Nascetti, "Sentinel-2 MSI data for active fire detection in major fire-prone biomes: A multi-criteria approach," *Int. J. Appl. Earth Observ. Geoinf.*, vol. 101, Sep. 2021, Art. no. 102347, doi: 10.1016/j.jag.2021.102347.

[13] G. Mazzeo, A. Falconieri, C. Filizzola, N. Genzano, N. Pergola, and F. Marchese, "Wildfire detection and mapping by satellite with an enhanced configuration of the normalized hotspot indices: Results from Sentinel-2 and Landsat 8/9 data integration," *IEEE Trans. Geosci. Remote Sens.*, vol. 63, 2025, Art. no. 5606121, doi: 10.1109/TGRS.2025.3528641.

[14] L. Giglio et al., "Active fire detection and characterization with the advanced spaceborne thermal emission and reflection radiometer (ASTER)," *Remote Sens. Environ.*, vol. 112, no. 6, pp. 3055–3063, Jun. 2008, doi: 10.1016/j.rse.2008.03.003.

[15] J. Ju et al., "The harmonized Landsat and Sentinel-2 version 2.0 surface reflectance dataset," *Remote Sens. Environ.*, vol. 324, Jul. 2025, Art. no. 114723.

[16] G. H. de Almeida Pereira, A. M. Fusioka, B. T. Nassu, and R. Minetto, "Active fire detection in Landsat-8 imagery: A large-scale dataset and a deep-learning study," *ISPRS J. Photogramm. Remote Sens.*, vol. 178, pp. 171–186, Aug. 2021, doi: 10.1016/j.isprsjprs.2021.06.002.

[17] A. Rostami, R. Shah-Hosseini, S. Asgari, A. Zarei, M. Aghdami-Nia, and S. Homayouni, "Active fire detection from Landsat-8 imagery using deep multiple kernel learning," *Remote Sens.*, vol. 14, no. 4, p. 992, Feb. 2022.

[18] A. M. Al-Dabbagh and M. Ilyas, "Uni-temporal Sentinel-2 imagery for wildfire detection using deep learning semantic segmentation models," *Geomatics, Natural Hazards Risk*, vol. 14, no. 1, Dec. 2023, Art. no. 2196370, doi: 10.1080/19475705.2023.2196370.

[19] X. Gao, W. Shi, M. Zhang, and L. Wang, "DAFDM: A discerning deep learning model for active fire detection based on Landsat-8 imagery," *IEEE J. Sel. Topics Appl. Earth Observ. Remote Sens.*, vol. 18, pp. 7982–8000, 2025.

[20] H. Liang, C. Zheng, X. Liu, Y. Tian, J. Zhang, and W. Cui, "Super-resolution reconstruction of remote sensing data based on multiple satellite sources for forest fire smoke segmentation," *Remote Sens.*, vol. 15, no. 17, p. 4180, Aug. 2023.

[21] Y. Liu, W. Zhi, B. Xu, W. Xu, and W. Wu, "Detecting high-temperature anomalies from Sentinel-2 MSI images," *ISPRS J. Photogramm. Remote Sens.*, vol. 177, pp. 174–193, Jul. 2021, doi: 10.1016/j.isprsjprs.2021.05.008.

[22] X. Huang, J. Yang, W. Wang, and Z. Liu, "Mapping 10-m global impervious surface area (GISA-10m) using multi-source geospatial data," *Earth Syst. Sci. Data Discuss.*, vol. 2022, pp. 1–39, Apr. 2022.

[23] Z. Liu, H. Tang, F. Lin, and S. Lyu, "CBRA: The first multi-annual (2016–2021) and high-resolution (2.5 m) building rooftop area dataset in China derived with super-resolution segmentation from Sentinel-2 imagery," *Earth Syst. Sci. Data Discuss.*, vol. 2023, pp. 1–40, May 2023.

[24] Y. Chen, J. Zhou, Y. Ge, and J. Dong, "Uncovering the rapid expansion of photovoltaic power plants in China from 2010 to 2022 using satellite data and deep learning," *Remote Sens. Environ.*, vol. 305, May 2024, Art. no. 114100.

[25] C. Jun, Y. Ban, and S. Li, "Open access to Earth land-cover map," *Nature*, vol. 514, no. 7523, p. 434, Oct. 2014.

[26] X. Huang, M. Li, J. Li, and Y. Song, "A high-resolution emission inventory of crop burning in fields in China based on MODIS thermal anomalies/fire products," *Atmos. Environ.*, vol. 50, pp. 9–15, Apr. 2012, doi: 10.1016/j.atmosenv.2012.01.017.

[27] M. Drusch et al., "Sentinel-2: ESA's optical high-resolution mission for GMES operational services," *Remote Sens. Environ.*, vol. 120, pp. 25–36, May 2012.

[28] Y. J. Kaufman et al., "Fire and smoke observed from the Earth Observing System MODIS instrument-products, validation, and operational use," *Int. J. Remote Sens.*, vol. 24, no. 8, pp. 1765–1781, Jan. 2003.

[29] L. Giglio, W. Schroeder, and C. O. Justice, "The collection 6 MODIS active fire detection algorithm and fire products," *Remote Sens. Environ.*, vol. 178, pp. 31–41, Jun. 2016.

[30] W. Schroeder et al., "Validation of GOES and MODIS active fire detection products using ASTER and ETM+ data," *Remote Sens. Environ.*, vol. 112, no. 5, pp. 2711–2726, May 2008, doi: 10.1016/j.rse.2008.01.005.

[31] M. J. L. García and V. Caselles, "Mapping burns and natural reforestation using thematic mapper data," *Geocarto Int.*, vol. 6, no. 1, pp. 31–37, Mar. 1991.

[32] T. Zhang, M. J. Wooster, and W. Xu, "Approaches for synergistically exploiting VIIRS I- and M-band data in regional active fire detection and FRP assessment: A demonstration with respect to agricultural residue burning in eastern China," *Remote Sens. Environ.*, vol. 198, pp. 407–424, Sep. 2017.

[33] R. G. Congalton, "A review of assessing the accuracy of classifications of remotely sensed data," *Remote Sens. Environ.*, vol. 37, no. 1, pp. 35–46, Jul. 1991.

[34] F. Li, X. Zhang, S. Kondragunta, C. C. Schmidt, and C. D. Holmes, "A preliminary evaluation of GOES-16 active fire product using Landsat-8 and VIIRS active fire data, and ground-based prescribed fire records," *Remote Sens. Environ.*, vol. 237, Feb. 2020, Art. no. 111600.

[35] C. Ichoku and Y. J. Kaufman, "A method to derive smoke emission rates from MODIS fire radiative energy measurements," *IEEE Trans. Geosci. Remote Sens.*, vol. 43, no. 11, pp. 2636–2649, Nov. 2005.

[36] J. T. Morisette et al., "Validation of MODIS active fire detection products derived from two algorithms," *Earth Interact.*, vol. 9, no. 9, pp. 1–25, Jul. 2005.

Lu Gui received the M.S. degree from China University of Geosciences, Wuhan, China, in 2022. She is currently pursuing the Ph.D. degree with the School of Geography and Information Engineering, China University of Geosciences, Wuhan, with a focus on the research of wildfire detection and emissions.

Rong Li received the Ph.D. degree in cartography and geographic information system from Chinese Academy of Sciences (CAS), Beijing, China, in 2015.

She is currently an Associate Professor with the College of Resources and Environment, Hubei University, Wuhan. Her main research interests include environmental remote sensing and atmospheric environmental remote sensing inversion algorithms and applications.

Minghui Tao received the Ph.D. degree from Chinese Academy of Sciences (CAS), Beijing, China, in 2013.

He worked with the Institute of Remote Sensing and Digital Earth, CAS, from 2013 to 2017. Since 2018, he has been working with China University of Geosciences (CUG), Wuhan, China, where he is currently a Professor with the School of Geography and Information Engineering. He mainly engaged in satellite remote sensing and atmospheric environment research, including atmospheric environmental remote sensing inversion algorithms, deep learning remote sensing, geographic information system (GIS) development, and application.

Zhe Jiang received the Ph.D. degree from Chinese Academy of Sciences (CAS), Beijing, China, in 2012.

Since 2015, she has been working with the Institute of Atmospheric Physics, CAS, as an Associate Researcher. She mainly engaged in thermal anomaly monitoring, aerosol scattering, and radiative forcing.

Lunche Wang received the M.S. and Ph.D. degrees in geography and photogrammetry and remote sensing from Wuhan University, Wuhan, China, in 2012 and 2015, respectively.

He is a Professor with the School of Geography and Information Engineering, China University of Geosciences, Wuhan, China. His research interests include climate change and remote sensing of the environment.

Jun Wang (Senior Member, IEEE) received the Ph.D. degree in atmospheric sciences from the University of Alabama-Huntsville, Huntsville, AL, USA, in 2005.

He is currently a Professor and the Chair of the Department of Chemical and Biochemical Engineering, The University of Iowa, Iowa City, IA, USA. He also serves as a James E. Ashton Professorship in engineering, and an Assistant Director, Iowa Technology Institute, Iowa City. He mainly engaged in interaction between atmospheric composition and climate change; impacts of aerosols on air quality, weather, and climate. His research related to cloud and trace gases, air quality and public health, irrigation, land use, fire, agriculture, and climate change, as well as renewable (solar and wind) energy.

Jiaxin Huang received the B.S. degree from Hubei University, Wuhan, China, in 2023. He is currently pursuing the Ph.D. degree with the School of Geography and Information Engineering, China University of Geosciences, Wuhan, with a focus on the research of anthropogenic emission sources.

Yi Wang received the Ph.D. degree in geoinformatics from the University of Iowa, Iowa City, IA, USA, in 2021.

He joined the University of Iowa, as a Post-Doctoral Research Scholar. He is currently a Professor with the School of Geography and Information Engineering, China University of Geosciences, Wuhan, China. He is mainly engaged in research related to remote sensing and modeling of the atmospheric environment, including satellite remote sensing of aerosols, assimilation of atmospheric environment satellite data, inversion of pollution source emission inventory, and deep learning of atmospheric environment models.

Liangfu Chen received the Ph.D. degree in geography from the Institute of Remote Sensing and Geographical Information System, Peking University, Beijing, China, in 1999.

Currently, he is a Professor with the Institute of Remote Sensing Applications, Chinese Academy of Sciences, Beijing. Since 2004, he has led an 863 project of China "Multisource Satellite Remote Sensing Technology of Atmospheric Pollution Monitoring," and the Knowledge Innovation Program, Chinese Academy of Sciences, Beijing His research includes the retrieval and application of atmosphere aerosol and trace gases based on remote sensing data.

Santo V. Salinas received the Ph.D. degree from Georg-August-Universität Göttingen, Göttingen, Germany, in 2003.

Currently, he is a Senior Research Scientist with the Centre for Remote Imaging, Sensing and Processing (CRISP), National University of Singapore (NUS), Singapore. He is a Principal Investigator for NASA's AERONET and MPLNET, Singapore, and has concurrent research projects and collaborations with NRL/NASA and other regional scientists. He specializes in satellite remote sensing, radiative transfer, atmospheric radiation, aerosols and clouds, and atmospheric modeling (aerosol dispersion and numerical weather prediction).